CHAIN OF TIME: IN-CONTEXT PHYSICAL SIMULATION WITH IMAGE GENERATION MODELS

YingQiao Wang*1,3, Eric Bigelow*1,4, Boyi Li^{5,6}, Tomer Ullman^{1,2}

ABSTRACT

We propose a novel cognitively-inspired method to improve and interpret physical simulation in vision-language models. Our "Chain of Time" method involves generating a series of intermediate images during a simulation, and it is motivated by in-context reasoning in machine learning, as well as mental simulation in humans. Chain of Time is used at inference time, and requires no additional finetuning. We apply the Chain-of-Time method to synthetic and real-world domains, including 2-D graphics simulations and natural 3-D videos. These domains test a variety of particular physical properties, including velocity, acceleration, fluid dynamics, and conservation of momentum. We found that using Chain-of-Time simulation substantially improves the performance of a state-of-the-art image generation model. Beyond examining performance, we also analyzed the specific states of the world simulated by an image model at each time step, which sheds light on the dynamics underlying these simulations. This analysis reveals insights that are hidden from traditional evaluations of physical reasoning, including cases where an image generation model is able to simulate physical properties that unfold over time, such as velocity, gravity, and collisions. Our analysis also highlights particular cases where the image generation model struggles to infer particular physical parameters from input images, despite being capable of simulating relevant physical processes.

1 Introduction

Recent developments in image generation models (IGMs) allow them to generate more complex, realistic, and coherent images Chen et al. (2025); Cao et al. (2025); Liu et al. (2023); Lu et al. (2024). But despite this improvement, these images often have distinct flaws, and may fail to capture real-world structures that are obvious to humans. Understanding the inner workings of Vision-Language Models (VLMs) and their internal world model representations has become a major topic in contemporary AI research (Dang et al., 2024; Chang et al., 2024; Goh et al., 2021; Bhalla et al., 2024; Zhang et al., 2024). In particular, there is a pressing question of how well VLMs and image generation models represent physical properties which are required to predict how world states unfold over time. In this work, we present a method for enhancing this physical reasoning ability in image generation models, which also allows us to analyze the step-by-step process that the models use to simulate physics over time.

Prior work provides a number of tools for evaluating the physical reasoning abilities of VLMs. Comprehensive benchmarks such as PhysBench (Chow et al., 2025) and WM-ABench (Gao et al., 2025) test VLMs on a wide array of physical simulation capabilities. Beyond VLMs, Meng et al. (2024) evaluates the extent to which text-to-image models – which generate images but do not take images as input – can generate images matching relational and physical constraints, using a separate VLM as an evaluator. While highly useful, such benchmarks do not answer the question of precisely how VLMs accomplish physical simulation. Our work aims to address this issue, providing a detailed analysis of the incremental processes underlying physical simulation. This work is, to our knowledge, unique in studying physical reasoning abilities of VLMs through Image Generation Models (IGMs),

¹Department of Psychology, Harvard University, ²Center for Brain Science, Harvard University

³Sakana AI, ⁴NTT Research, ⁵Department of Computer Science, UC Berkeley

⁶Nvidia Research, *Equal contribution

^{*}Correspondence to: yingqiaowang@g.harvard.edu, ebigelow@g.harvard.edu

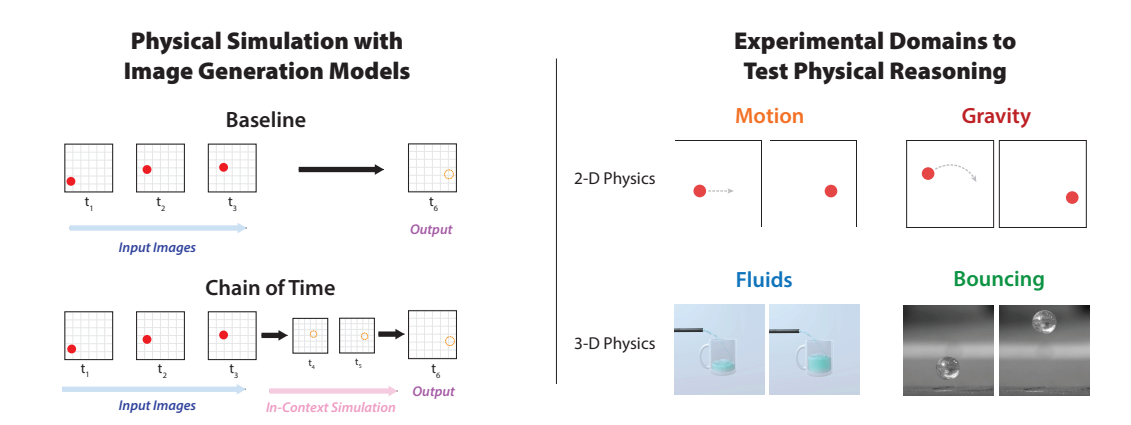


Figure 1: (Left, Top) We study physical reasoning in multi-modal image generation models by providing the model a sequence of input images showing a scene in subsequent time steps, and having the model generate an image that simulates what the scene will look like some time in the future. Accurately predicting future world states requires reasoning about physical properties. (Left, Bottom) Our method, Chain of Time, allows these models to simulate a sequence of images in-context, generating one image at a time, with the last image representing the final prediction of the scene. (Right) We use four experimental domains designed to test models' ability to reason about specific physical properties: Velocity, Gravity, Fluid Dynamics, and Collision.

which take images and text as input and generate images as output. Given the fact that IGMs are becoming native to vision-language models (OpenAI, 2025), evaluating image generation models may also provide valuable insights into the inner workings of VLMs.

In this work, we adopt a theoretical framework of mental simulation from cognitive science to understand physical reasoning and simulation abilities in Image Generation Models (Section 2). This framework helps us understand how IGMs reason about physical processes that unfold over time, by mapping input images to a latent state which is simulated with a Markov process to predict future time steps. In order to both improve physical the reasoning ability of IGMs, and to expose an interpretable trace of intermediate reasoning steps, we propose a novel method for in-context physical simulation, which we call Chain of Time (Section 3, Fig. 1). We test a state-of-the-art IGM with physical reasoning in four experimental domains, including two 2-D and two 3-D domains, which test four sets of physical properties: motion, gravity, fluid dynamics, and collisions. We find that Chain of Time enhances the IGM's physical reasoning abilities, enabling it to generate images that are more accurate across several specific metrics. We also provide a novel analysis of the step-by-step process by which an IGM may simulates the physical world, and draw insights about what aspects of the process it succeeds and struggles with.

2 Mental Simulation in Humans

People can reason efficiently about the physical dynamics of everyday objects. For example, if you saw a pitcher full of juice begin to fall off of a table, you might quickly and intuitively predict what sequence of events will happen next. There are many competing theories that try to explain this 'intuitive physics'. One current proposal is that people rely on an 'internal physics engine' to carry out a mental simulation of a given scene (Battaglia et al., 2013; Ullman et al., 2017). While this proposal has its critiques (see for example Ludwin-Peery et al. (2021)), it finds support in cognitive science, computational modeling, cognitive development, and neuroscience (Fischer et al., 2016; Gerstenberg & Stephan, 2021; Allen et al., 2021; Fischer, 2021; Bass et al., 2021; Balaban & Ullman, 2025). More recent work suggests it is likely that humans combine various computations to carry out physical reasoning, mental simulation being just one component Hartshorne & Jing (2025); Sosa et al. (2025); Smith et al..

Given that current research suggests that step-by-step mental simulation is an important component in human physical reasoning, we adopt its formalism for studying (and potentially improving upon) the physical reasoning of current IGMs. For our purposes here, we consider a basic version of the mental

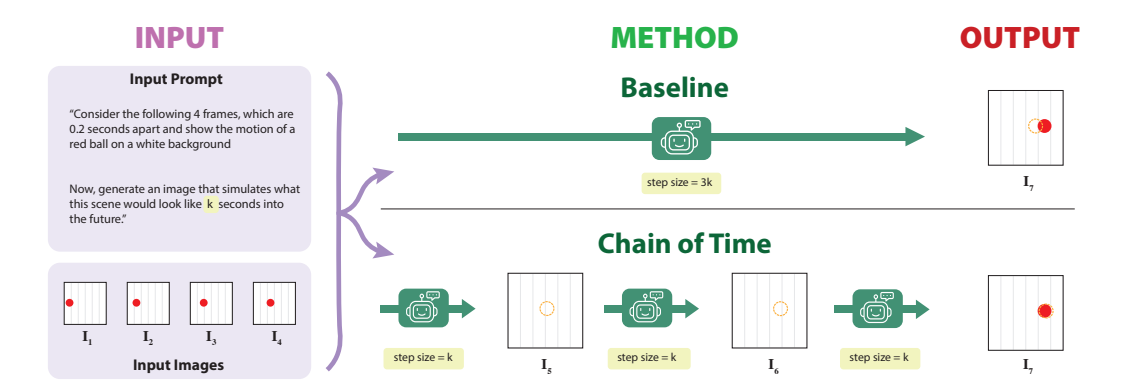


Figure 2: In our paradigm, we give an IGM a sequence of input images, along with a prompt instructing the model to simulate the scene into the future for a specified length of time (Left). As a baseline, Direct Prediction (Middle, Top) directly predicts the final state (Right) without intermediate steps. We propose a novel method, Chain of Time (Middle, Bottom), which instead generates a sequence of images corresponding to a step-by-step simulation of the scene on the way to the predicted final state, with each mid-point image serving as input and output in mid-point computation.

physics engine framework: Suppose that an agent observes an image I that describes a scene at time t in a pixel-based format, and wants to predict the state of the scene at a later time. A mental physics engine is a probabilistic transition function that can achieve this by composing three sub-functions: de-renderer ϕ , simulator τ , and (optionally) renderer ϕ^{-1} . The engine takes in the current image I_t , and de-renders it into the state of the world at that time, X_t . The engine then applies dynamic update rules to that state, corresponding to a transition τ that produces a distribution over future states of the world X_{t+1} . The engine may then render the state of the world back into a predicted image I_{t+1} .

A few notes on this overall formulation: First, while de-rendering has been studied in the context of intuitive physics in the past (e.g. Wu et al., 2017a;b; Smith et al., 2019), many other techniques exist for going from observations to physical states, and for our purposes here the specific technique is of less importance. Second, while the images I are pixel-based, the underlying physical state X is not, and corresponds to the 'game state' that describes in a lower-dimensional way the position, identity, and physical parameters of objects (Smith et al., 2019). Third, in computer graphics it is not strictly necessary to render the state of the world back into an image in order to answer various questions about the state, something that may hold for human mental physics as well (Balaban & Ullman, 2025).

To put it more formally, the mental simulation formalism we consider here is:

$$\begin{array}{ll} p(X_t \mid I_t) = \phi(I_t) + N(0, \sigma_{\phi}) & \text{De-rendering} \\ p(X_{t+1} \mid X_t) = \tau(X_t) + N(0, \sigma_{\tau}) & \text{Simulation} \\ p(I_{t+1} \mid X_{t+1}) = \phi^{-1}(X_{t+1}) + N(0, \sigma_{\phi^{-1}}) & \text{Rendering} \end{array}$$

The noise parameters σ_{ϕ} , σ_{τ} , and σ_{ϕ^1} account for perceptual noise in the de-rendering of I, the cognitive complexity of mental simulation of the underlying state X, and imperfect imagery in the rendering of the state back to an image.

Notice that the state and scene at timestep t+1 depend only on the previous state and scene at timestep t. So, the formalism defines a linearly unfolding Markov Chain, that moves from an initial observation I_0 step-by-step to a final state at time T, X_T , and optionally the predicted image at that time, I_T . While such step-by-step computations may underlie human mental simulation, it remains unclear whether current IGMs tasked with predicting the future state of a scene I at time T also go through a step-by-step simulation. Nevertheless, even if current models do not do so on their own, this framework suggests a method for bringing them more in line with human-like reasoning, which we turn to next.

3 CHAIN-OF-TIME SIMULATION

Chain-of-Time simulation is inspired by two bodies of prior literature: the cognitive science of mental simulation (described briefly in Section 2), and in-context reasoning in LLMs. Incontext reasoning methods with LLMs coerce a model to spell out intermediate reasoning steps in its output stream, before giving a final answer. This may be through prompting, as in Chainof-Thought reasoning (Kojima et al., 2022), or through specialized training regimes (Guo et al., 2025; Jaech et al., 2024). These methods can significantly improve LLM performance on a variety of tasks, extending the ability of LLM to reason over complex problems with many individual steps. These reasoning chains are also distinct from traditional LLM tasks, since intermediate steps can be directly inspected by humans to interpret what the model is doing. Although in some cases a model's intermediate reasoning tokens may not align with its final an-

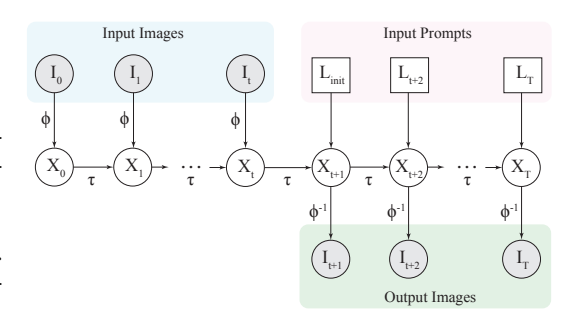


Figure 3: Chain of Time is a composition of three components: De-rendering ϕ , Simulation τ , and Rendering ϕ^{-1} . De-rendering operates by converting input images $I_0 \dots I_t$ into world states X_t , which represent a physical simulation over time. Chain of Time begins with an initial prompt L_{init} and iteratively generates a sequence of in-context output images $I_{t+1} \dots I_T$ with follow-up prompts $L_{t+1} \dots L_T$

swer (Turpin et al., 2023), Chain of Thought reasoning has proved a valuable tool for auditing the behavior of language models. Various theories have been developed to try to explain precisely why and how these methods work or occasionally fail (Wang et al., 2022; Merrill & Sabharwal, 2023; Prystawski et al., 2023).

Based on the prior literature in human mental simulation and in-context reasoning, we propose a novel method for improving physical reasoning with in-context simulations. We call this method Chain-of-Time simulation (Figure 1). We treat VLMs as a derenderer ϕ and a simulator τ , and the IGMs as a renderer ϕ^{-1} . The basic physical simulation task we consider is as follows: given a sequence of input images $I_{0:t}$ up to a given time t, generate a new image \widehat{I}_{t+k} that accurately depicts what the scene will look like k time steps into the future. Chain-of-Time simulation involves two prompts (provided in Appendix B): first, a Simulation Instruction prompt that, along with a sequence of input images, instructs the model to simulate an image k seconds into the future. After the IGM generates a single image, we continue with our Simulation Follow-up prompt, which instructs the model to generate another image simulated an additional k seconds into the future until t+k=T. In our experiments, we used T=t+0.8 sec and sub-steps $s\in\{0.2\,\sec,0.4\,\sec,0.8\,\sec\}$, where we instruct the model to generate another image every s seconds after time t, until it reaches time t. To capture the Direct Prediction baseline, we use a method equivalent to Chain of Time but with a single timestep, prompting the IGM to predicts \hat{I}_{t+k} given $I_{0:t}$, without intermediate prompts. In our case, to match the Chain of Time parameters, we use $k=0.8\,\sec$ as the Direct Prediction baseline.

3.1 Previous Work

Prior work has developed in-context reasoning methods for VLMs that use images instead of language to represent individual reasoning steps. Our method differs from these approaches in a few important ways. Hu et al. (2024) proposed a method to solve simple reasoning problems with a VLMs, such as geometry and spatial reasoning, and individual steps involve interleaved images and text outputs. Similar to our method, this approach requires no additional training. However, in contrast with Chain-of-Time, this method is a separate tool that the VLM evokes, which uses LLM code generation along with a Python interpreter to render intermediate sketches. Xu et al. (2025) proposed a method for planning in which a VLM is explicitly trained with reinforcement learning to generate sequences of images to solve tasks such as maze navigation. Chain-of-Time simulation, on the other hand, strives to improve physical simulation with IGMs where "steps" correspond to units of time, rather than planning, where "steps" correspond to actions an agent takes in an environment. Our method also differs in that it can be applied to out-of-the-box IGMs with no additional training. Further, our work presents an in-depth analysis of the sequence of images generated by Chain-of-Time, where we consider the accuracy of simulation at each individual step. Such an analysis was not used in Hu

et al. (2024) or Xu et al. (2025), although Xu et al. (2025) develops learning metrics that evaluate step-wise accuracy, and both works show examples of generated image sequences.

4 EXPERIMENTS

We hypothesize that by using Chain of Time, IGMs will be able to achieve better accuracy than when using direct prediction. We use the frames created by IGMs using Chain-of-Time simulation to reveal the details about the simulation, including the initial states estimated by IGMs, physical interactions, and physical motion simulated by IGMs. To examine the overall validity and applicability of our method, we tested Chain-of-Time on both **2D Physics** and **3D Physics**, and four domains: **2D Motion**, **2D Gravity**, **Fluids**, and **Bouncing**. We analyzed our results in two ways: first, we measured the accuracy of predicted images relative to ground truth; and second, we visualized the temporal dynamics in simulated images (such as x and y location) to assess physical parameters in the IGM's simulations (such as velocity and acceleration).

4.1 EXPERIMENTAL SETUP

Stimuli Design As mentioned above, we used 4 different physical domains as our stimuli: 2D Motion, 2D Gravity, Fluids, and Bouncing. The stimuli used in 2D physics (2D Motion, 2D Gravity) were created in a simulation environment, and resemble stimuli in previous studies of intuitive physics Smith & Vul (2013), Bass et al. (2021), Gerstenberg & Stephan (2021). The stimuli used in 3D physics category (Fluids) were borrowed from Wang & Ullman (2025). We manipulated the physical parameters used to generate stimuli in the 2D physics category (2D Motion, 2D Gravity) and 3D physics category (Fluids) by changing the simulation parameters used generate the stimuli. In the Bouncingdomain, we used real-world stimuli which have different physical parameters, i.e. different balls with different levels of "bounciness", and we simulated different speeds by re-sampling input videos at different frame rates. For further details of how we designed stimuli, please refer to Appendix A.

Experimental Procedure We used OpenAI's GPT4-0 (gpt-image-1 ¹) as the Image Generation Model in our experiment, as of September, 2025. We also empirically tested other image generation models including DALLE-3, but found that these models were unable to simulate images of future world states with any reasonable accuracy. In order to analyze the content of generated images, we use a collection of domain-specific algorithms to identify object locations, for example the (x, y) coordinates of objects, and the heights of water levels for fluids. These algorithms use simple tools from classic computer vision such as Hough transforms, and are further described in Appendix C.3.

At the start of each trial, the model was given 5 frames of a stimulus, showing the scene at 0, 0.2, 0.4, 0.6, and 0.8 seconds. Given these 5 frames, the model was asked to generate simulated frames at a time in the future, following the Initial Simulation Prompt. If Chain-of-Time 0.2s or Chain-of-Time 0.4s were used (see below), additional frames were generated following the Simulation Follow-Up Prompt. Details of the prompts we used can be found in Appendix B.

Sampling Details Chain of Time generates frames at different precision, depending on a frame-rate parameter s. We considered two versions of Chain-of-Time with s=0.2 sec and s=0.4 sec. Since the final frame was 0.8 seconds into the future, Chain-of-Time with s=0.2 sec generated 4 frames (corresponding to 0.2, 0.4, 0.6, and 0.8 seconds into the future). Chain-of-Time with s=0.4 sec generated 2 frames (corresponding to 0.4 and 0.8 seconds into the future). In addition, we had a baseline termed "Direct Prediction". In this method, we asked the model to directly generate the requested final frame, which is 0.8 seconds into the future.

For 2D Motion, we ran each stimulus 5 times (N=5) across all Chain-of-Time simulations and Direct Prediction. For 2D Gravity, we ran each stimulus 20 times (N=20) across all Chain-of-Time simulations and Direct Prediction. For Fluids and Bouncing domain, we ran each stimulus 10 times (N=10) across all Chain-of-Time simulations and Direct Prediction.

lopenai.com/index/image-generation-api/

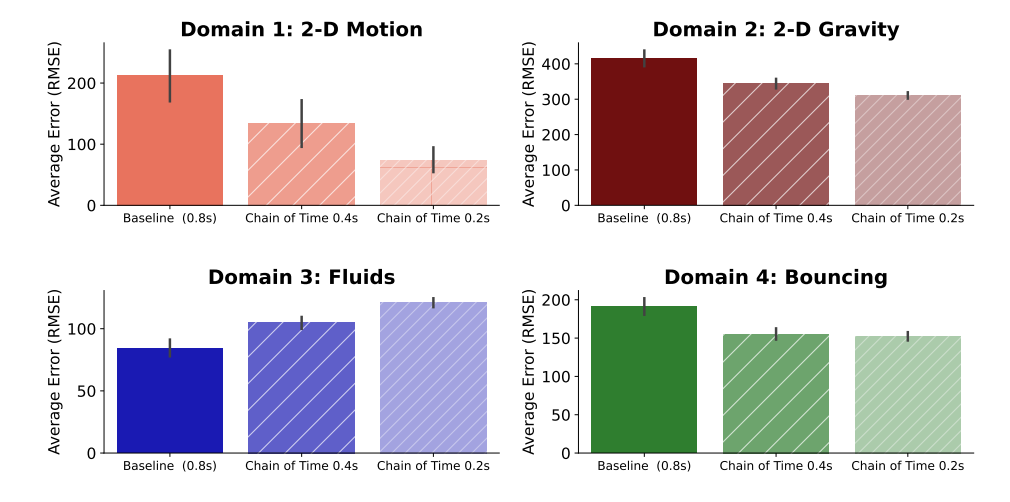


Figure 4: Prediction errors for all four domains, averaged across all data for each domain. Prediction error is measured by taking the average RMSE between the ground-truth positions (location of focal object, or water level) and the positions predicted by the IGM. Error bars are 95% CI. We generally find a monotonic relationship between Chain-of-Time precision and performance. In the case of Fluids, we observe that the initial state simulated by the IGM is inaccurate, and this error compounds with increasing degrees of simulation, see Section 5.2.2 for detailed analysis.

5 RESULTS

5.1 ACCURACY ANALYSIS

We evaluated the IGM's accuracy in predicting the ground-truth position of the variable of interest (object location or water height) under three methods: Chain-of-Time (0.2), Chain-of-Time (0.4), and Direct Prediction. As shown in Figure 4, using a finer Chain-of-Time step generally improves accuracy in three of the four domains. In 2D Motion, Chain-of-Time (0.2) more than halves the error relative to Direct Prediction. These results indicate that Chain-of-Time can improve prediction accuracy for both 2D and 3D tasks.

In Fluids, Chain-of-Time enables the IGM to simulate fluid dynamics, but errors in the estimated physical parameters prevent performance gains: as the frame-rate s decreases, the error increases. We examine potential causes of this behavior in the following section.

5.2 PHYSICAL PARAMETER AND PHYSICAL MOTION ANALYSIS

In 2D Motion, the IGM successfully simulates the simplest motion which is a simple forward rolling motion, and Chain-of-Time (0.2 s) achieves the lowest root-mean-square error (RMSE). Building on this initial result, we next examine the IGM's ability to simulate more complex physical interactions and motions in 2D Gravity, Fluids, and Bouncing.

By design, Chain-of-Time yields simulated images going from t+s to T, where the intermediate steps are denoted as $I_{t:T}$. As described in Section 4, we generated $I_{t:T}$ using step sizes of 0.2s and 0.4s. We then used these sequences to infer (i) the physical parameters as perceived by the model, (ii) the physical interactions, and (iii) the simulated motion. In each subsection, we present a single trial as a running example; additional stimuli and replications across all four domains appear in Appendix D. Unless noted otherwise, we focus on Chain-of-Time (0.2), which provides the highest temporal resolution and the largest number of intermediate frames. Results for Chain-of-Time (0.4) are provided in Appendix D.

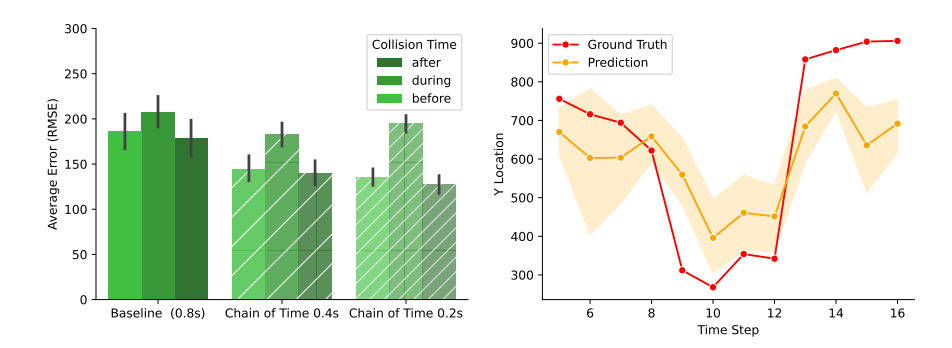


Figure 5: (Left) Prediction error rate across methods and time periods. In the collision domain, we find lower error rates in image model predictions for periods before and after the bouncing collision, compared with time periods during which the collision occurs. This disparity increases with Chain of Time, since performance improves for the before/after periods, but error remains high for the collision time period. (Right) Simulated ball location (orange) using Chain-of-Time 0.2s in the Bouncing domain follow a similar U-shaped curve as the ground truth ball location (red). Ball locations are shown here for a single video (orange), with predictions aggregated across all samples for the three time periods (before/during/after collision).

5.2.1 IMAGE GENERATION MODELS CAN PRODUCE IMAGES CORRESPONDING TO 2D AND 3D PHYSICAL MOTIONS AND INTERACTIONS

Across all three domains, the IGM, when run with Chain-of-Time step sizes of 0.2 s and 0.4 s, generally produced image sequences consistent with simulations of the domain-specific physical motions and interactions.

In 2D Gravity, we evaluated the IGM's ability to simulate projectile motion, where gravity produces a curved (parabolic) trajectory. For illustration, we analyzed a stimulus with initial speed 230, a launch angle of 60° , and a bottom-left launch position. As shown in Figure 6, the IGM reproduced the projectile's curved path and closely tracked the ground truth. Decomposing the 2D trajectory into its x- and y-components (time series in Figure 6) showed that, under Chain-of-Time step sizes of $0.2\,\mathrm{s}$ and $0.4\,\mathrm{s}$, the x-position increased approximately linearly, while the y-position rose to a peak and then decreased under constant downward acceleration—consistent with projectile motion under gravity.

In Fluids, we evaluated whether the IGM can simulate fluid dynamics. Although Section 5.1 reports higher average error for Chain-of-Time step sizes of $0.2\,\mathrm{s}$ and $0.4\,\mathrm{s}$, the model nevertheless reproduces the expected qualitative behavior: the water level rises as the simulation progresses. As shown in Figure 7, the predicted water level increases over time. We analyze why the average error increases when Chain-of-Time is used in Section 5.2.2.

In Bouncing, we evaluated bouncing motion. We analyzed stimuli with a plastic ball and a medium coefficient of restitution. As shown in Figure 5, the IGM reproduces the expected qualitative behavior: the y-position decreases under gravity during free fall, and increases after ground contact as the ball rebounds. The figure also reveals a deviation between the ground-truth and IGM-predicted y trajectories, which we analyzed this discrepancy in Section 5.2.2.

5.2.2 IMAGE GENERATION MODELS SHOW PHYSICAL PARAMETER ESTIMATION ERROR FOR 3D PHYSICS SIMULATION

In Section 4, we observed that Chain-of-Time with step sizes of $0.2\,\mathrm{s}$ and $0.4\,\mathrm{s}$ exhibited higher average error than Direct Prediction in the fluid-dynamics domain. This motivated us to examine how the model perceives the initial state sequence $X_{0:t}$, which in the case of Fluidsincludes physical parameters such as flow rate and initial water level.

We analyzed the simulated image sequences $\widehat{I}_{t:T}$ generated by the IGM in Fluids. Specifically, we examined the predicted water-level time series for stimuli with slow (25 frames/s) and fast (75

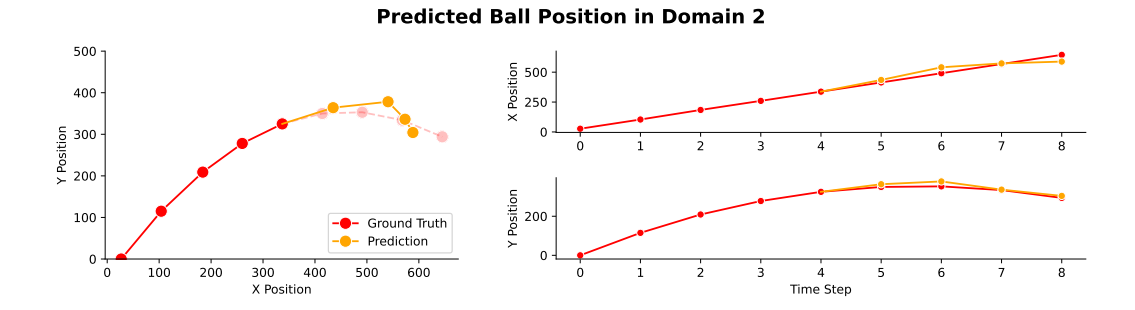


Figure 6: Predicted projectile position for 2D Gravity over time for a single trial using Chain-of-Time 0.2s. Red represents the ground truth ball location and orange is the simulated ball location at each time step, averaged across 20 samples. (Left) Projectile location in (x,y) coordinate space (Right) Predicted x-location and y-location as a function of time.

frames/s) flow rates, and with low (1/12 and 3/12 full) versus high (7/12 and 9/12 full) initial water levels. As shown in Figure 7, the IGM is sensitive to the initial water level—lowering the initial level shifts the intercept (dotted to solid line; left panel)—but largely insensitive to flow rate—the slope remains similar for 25 and 75 frames/s (right panel).

The sensitivity to the initial water level indicates that the IGM leverages salient visual cues in the inputs, whereas its insensitivity to flow rate suggests substantial error in estimating that parameter. Flow rate is a critical physical variable in this task, ensuring that the glass mugs are filled with the correct amount of water over time. These findings imply that errors in estimating the initial state $X_{0:t}$ can occur, especially for parameters that are not directly observable. Such estimation error accumulates over the rollout: as the Chain-of-Time step size k decreases (i.e., more, finer steps), the accumulated error grows. This explains why Chain-of-Time underperforms Direct Prediction in the fluid-dynamics domain, and why the $0.2 \, \mathrm{s}$ configuration performs worse than $0.4 \, \mathrm{s}$.

In Bouncing, we examined the model's ability to estimate a more complex physical parameter: the coefficient of restitution (or "bounciness") and its effect on the simulated trajectories. As noted in Section 5.2.1, we observe a deviation between the ground-truth and simulated positions between frames 10 and 16, collapsing between the three partitions (before, during, and after). This interval corresponds to the deformation phase (the *during* partition), when the ball contacts the ground, deforms, and rebounds. As shown in Figure 5, the slope of the simulated y-position trajectory

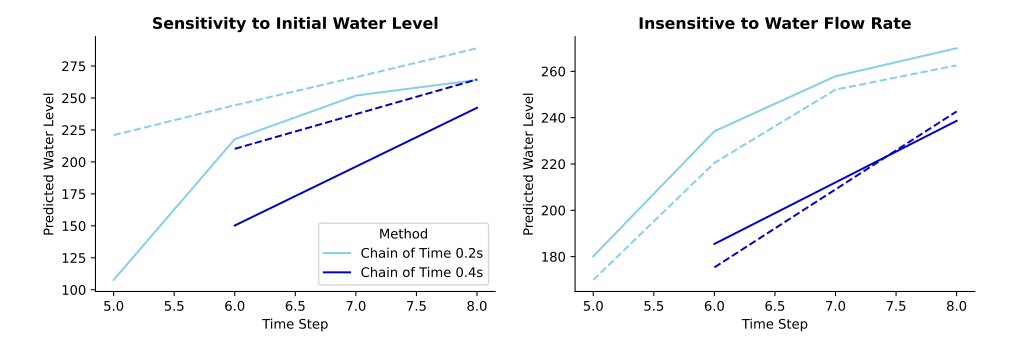


Figure 7: In the Fluids domain, we find that the IGMs are able to simulate water levels increasing over time. Here we show water levels in generated images steadily increasing as a function of time. (Left) The model is sensitive to initial water levels, with solid lines representing a low water level at the initial time of simulation t and dotted lines representing a high initial water level. (Right) However, the model is insensitive to the flow rate of water, with water level consistently increasing at the same rate during simulations. Solid lines represent a slow flow rate and dotted lines represent a t0 3x faster flow rate.

beginning at t=10 is markedly smaller than that of the ground truth, implying a slower rebound. This pattern is consistent with an underestimation of the coefficient of restitution.

Extending the analysis to all stimuli in Bouncing(Figure 5), the RMSE increases during the deformation (during) phase and is significantly higher than in the other two partitions for Chain-of-Time step sizes of $0.2\,\mathrm{s}$ and $0.4\,\mathrm{s}$. This finding further supports the conclusion that the IGM wrongly estimated the coefficient of restitution when simulating the deformation phase.

6 DISCUSSION

Motivated by mental simulation in humans and in-context reasoning in Large-Language Models, we presented a method for step-by-step physical simulation in Image Generation Models. In this Chain-of-Time method, a prediction is sliced into finer precision, with mid-point frames being fed as input to the next step in an unfolding systematic process. We assessed the Chain-of-Time method for differing degrees of precision, across different physical domains, using different quantitative and qualitative metrics, including overall accuracy compared to ground truth, and the recovery of physical parameters.

Our results suggest that while an Image Generation Model may potentially have some degree of physical simulation when paired with a VLM. Our Chain-of-Time method, inspired by the mental simulation theory in humans, can improve this ability, which is shown by the improved accuracy in various physical tasks when Chain-of-Time method is deployed. When using this method, we can assess the simulated images produced by the image model, and probe the model's perception over critical physical parameters, physical motions, and physical interactions. We found that the model is capable of simulating both 2D and 3D physical motions and interactions. But, the model has various problems when simulating 2D and 3D physics, including slowing down the simulation when 2D physics is simulated, or estimating the wrong physical parameters when 3D physics is simulated.

Our work is one step towards a more general method of step-by-step simulation in image generation models, and many open questions and directions of research remain. For example, while we considered several settings of the precision (time-step k), there is a trade-off between the potential accuracy gained by better precision, and the resulting drain on computational resources. The precision that corresponds to the optimal trade-off is left for further exploration, and may depend on the target domain. In addition, we found that greater precision can *compound* error, if the initial parameters are not correctly measured or observed, and finding a way to assess this independently to know whether Chain of Time will be beneficial is another avenue for future work. More generally, we see great value in using Chain of Time to examine other aspects of physical reasoning not directly touched on here, including judgments of causality and non-simulation-based physical reasoning such as heuristics and abstractions. Also, while our work was inspired by research examining mental simulation in humans, our Chain of Time method and the results offers suggestions in the reverse direction for further study in people. To be specific, while much of the work on mental simulation assumes people unfold a physical scene step-by-step, the exact step-size and its possible consequences is mostly left unexamined.

REFERENCES

- Kelsey R Allen, Kevin A Smith, Laura-Ashleigh Bird, Joshua B Tenenbaum, Tamar R Makin, and Dorothy Cowie. Lifelong learning of cognitive strategies for physical problem-solving: the effect of embodied experience. *bioRxiv*, pp. 2021–07, 2021.
- Halely Balaban and Tomer D Ullman. Physics versus graphics as an organizing dichotomy in cognition. *Trends in Cognitive Sciences*, 2025.
- Ilona Bass, Kevin A Smith, Elizabeth Bonawitz, and Tomer D Ullman. Partial mental simulation explains fallacies in physical reasoning. *Cognitive Neuropsychology*, 38(7-8):413–424, 2021.
- Peter W Battaglia, Jessica B Hamrick, and Joshua B Tenenbaum. Simulation as an engine of physical scene understanding. *Proceedings of the National Academy of Sciences*, 110(45):18327–18332, 2013.
- Usha Bhalla, Alex Oesterling, Suraj Srinivas, Flavio Calmon, and Himabindu Lakkaraju. Interpreting clip with sparse linear concept embeddings (splice). *Advances in Neural Information Processing Systems*, 37:84298–84328, 2024.
- Yuefan Cao, Xuyang Guo, Jiayan Huo, Yingyu Liang, Zhenmei Shi, Zhao Song, Jiahao Zhang, and Zhen Zhuang. Text-to-image diffusion models cannot count, and prompt refinement cannot help. *arXiv preprint arXiv:2503.06884*, 2025.
- Yupeng Chang, Xu Wang, Jindong Wang, Yuan Wu, Linyi Yang, Kaijie Zhu, Hao Chen, Xiaoyuan Yi, Cunxiang Wang, Yidong Wang, et al. A survey on evaluation of large language models. *ACM Transactions on Intelligent Systems and Technology*, 15(3):1–45, 2024.
- Sixiang Chen, Jinbin Bai, Zhuoran Zhao, Tian Ye, Qingyu Shi, Donghao Zhou, Wenhao Chai, Xin Lin, Jianzong Wu, Chao Tang, Shilin Xu, Tao Zhang, Haobo Yuan, Yikang Zhou, Wei Chow, Linfeng Li, Xiangtai Li, Lei Zhu, and Lu Qi. An empirical study of gpt-40 image generation capabilities, apr 2025. URL https://arxiv.org/abs/2504.05979. Version 2, revised 10 Apr 2025.
- Wei Chow, Jiageng Mao, Boyi Li, Daniel Seita, Vitor Guizilini, and Yue Wang. Physbench: Benchmarking and enhancing vision-language models for physical world understanding. *arXiv* preprint arXiv:2501.16411, 2025.
- Yunkai Dang, Kaichen Huang, Jiahao Huo, Yibo Yan, Sirui Huang, Dongrui Liu, Mengxi Gao, Jie Zhang, Chen Qian, Kun Wang, et al. Explainable and interpretable multimodal large language models: A comprehensive survey. *arXiv preprint arXiv:2412.02104*, 2024.
- Jason Fischer. The building blocks of intuitive physics in the mind and brain, 2021.
- Jason Fischer, John G Mikhael, Joshua B Tenenbaum, and Nancy Kanwisher. Functional neuroanatomy of intuitive physical inference. *Proceedings of the national academy of sciences*, 113 (34):E5072–E5081, 2016.
- Qiyue Gao, Xinyu Pi, Kevin Liu, Junrong Chen, Ruolan Yang, Xinqi Huang, Xinyu Fang, Lu Sun, Gautham Kishore, Bo Ai, et al. Do vision-language models have internal world models? towards an atomic evaluation. In *ICLR 2025 Workshop on World Models: Understanding, Modelling and Scaling*, 2025.
- Tobias Gerstenberg and Simon Stephan. A counterfactual simulation model of causation by omission. *Cognition*, 216:104842, 2021.
- Gabriel Goh, Nick Cammarata, Chelsea Voss, Shan Carter, Michael Petrov, Ludwig Schubert, Alec Radford, and Chris Olah. Multimodal neurons in artificial neural networks. *Distill*, 6(3):e30, 2021.
- Daya Guo, Dejian Yang, Haowei Zhang, Junxiao Song, Ruoyu Zhang, Runxin Xu, Qihao Zhu, Shirong Ma, Peiyi Wang, Xiao Bi, et al. Deepseek-r1: Incentivizing reasoning capability in llms via reinforcement learning. *arXiv preprint arXiv:2501.12948*, 2025.

- Joshua K Hartshorne and Mengguo Jing. Insights into cognitive mechanics from education, developmental psychology and cognitive science. *Nature Reviews Psychology*, pp. 1–15, 2025.
- Yushi Hu, Weijia Shi, Xingyu Fu, Dan Roth, Mari Ostendorf, Luke Zettlemoyer, Noah A Smith, and Ranjay Krishna. Visual sketchpad: Sketching as a visual chain of thought for multimodal language models. arXiv preprint arXiv:2406.09403, 2024.
- Aaron Jaech, Adam Kalai, Adam Lerer, Adam Richardson, Ahmed El-Kishky, Aiden Low, Alec Helyar, Aleksander Madry, Alex Beutel, Alex Carney, et al. Openai o1 system card. arXiv preprint arXiv:2412.16720, 2024.
- Takeshi Kojima, Shixiang Shane Gu, Machel Reid, Yutaka Matsuo, and Yusuke Iwasawa. Large language models are zero-shot reasoners. *Advances in neural information processing systems*, 35: 22199–22213, 2022.
- Qihao Liu, Adam Kortylewski, Yutong Bai, Song Bai, and Alan Yuille. Discovering failure modes of text-guided diffusion models via adversarial search. *arXiv preprint arXiv:2306.00974*, 2023.
- Wenquan Lu, Yufei Xu, Jing Zhang, Chaoyue Wang, and Dacheng Tao. Handrefiner: Refining malformed hands in generated images by diffusion-based conditional inpainting. In *Proceedings of the 32nd ACM International Conference on Multimedia*, pp. 7085–7093, 2024.
- Ethan Ludwin-Peery, Neil R Bramley, Ernest Davis, and Todd M Gureckis. Limits on simulation approaches in intuitive physics. *Cognitive Psychology*, 127:101396, 2021.
- Fanqing Meng, Wenqi Shao, Lixin Luo, Yahong Wang, Yiran Chen, Quanfeng Lu, Yue Yang, Tianshuo Yang, Kaipeng Zhang, Yu Qiao, et al. Phybench: A physical commonsense benchmark for evaluating text-to-image models. *arXiv preprint arXiv:2406.11802*, 2024.
- William Merrill and Ashish Sabharwal. The expressive power of transformers with chain of thought. *arXiv preprint arXiv:2310.07923*, 2023.
- OpenAI. Introducing 4o image generation, 2025. URL https://openai.com/index/introducing-4o-image-generation/.
- Ben Prystawski, Michael Li, and Noah Goodman. Why think step by step? reasoning emerges from the locality of experience. *Advances in Neural Information Processing Systems*, 36:70926–70947, 2023.
- Kevin Smith, Peter Battaglia, and Joshua Tenenbaum. Integrating heuristic and simulation-based reasoning in intuitive physics.
- Kevin Smith, Lingjie Mei, Shunyu Yao, Jiajun Wu, Elizabeth Spelke, Josh Tenenbaum, and Tomer Ullman. Modeling expectation violation in intuitive physics with coarse probabilistic object representations. *Advances in neural information processing systems*, 32, 2019.
- Kevin A Smith and Edward Vul. Sources of uncertainty in intuitive physics. *Topics in cognitive science*, 5(1):185–199, 2013.
- Felix A Sosa, Samuel J Gershman, and Tomer D Ullman. Blending simulation and abstraction for physical reasoning. *Cognition*, 254:105995, 2025.
- Miles Turpin, Julian Michael, Ethan Perez, and Samuel Bowman. Language models don't always say what they think: Unfaithful explanations in chain-of-thought prompting. *Advances in Neural Information Processing Systems*, 36:74952–74965, 2023.
- Tomer D Ullman, Elizabeth Spelke, Peter Battaglia, and Joshua B Tenenbaum. Mind games: Game engines as an architecture for intuitive physics. *Trends in cognitive sciences*, 21(9):649–665, 2017.
- Boshi Wang, Sewon Min, Xiang Deng, Jiaming Shen, You Wu, Luke Zettlemoyer, and Huan Sun. Towards understanding chain-of-thought prompting: An empirical study of what matters. *arXiv* preprint arXiv:2212.10001, 2022.
- YingQiao Wang and Tomer D Ullman. Resource bounds on mental simulations: Evidence from a liquid-reasoning task. *Journal of Experimental Psychology: General*, 2025.

- Jiajun Wu, Erika Lu, Pushmeet Kohli, Bill Freeman, and Josh Tenenbaum. Learning to see physics via visual de-animation. *Advances in neural information processing systems*, 30, 2017a.
- Jiajun Wu, Joshua B Tenenbaum, and Pushmeet Kohli. Neural scene de-rendering. In *Proceedings of the IEEE Conference on Computer Vision and Pattern Recognition*, pp. 699–707, 2017b.
- Yi Xu, Chengzu Li, Han Zhou, Xingchen Wan, Caiqi Zhang, Anna Korhonen, and Ivan Vulić. Visual planning: Let's think only with images. *arXiv preprint arXiv:2505.11409*, 2025.
- Jingyi Zhang, Jiaxing Huang, Sheng Jin, and Shijian Lu. Vision-language models for vision tasks: A survey. *IEEE transactions on pattern analysis and machine intelligence*, 46(8):5625–5644, 2024.

A STIMULI DESIGN AND SPECIFICATION OF THE STIMULI

A.1 2D Motion

The stimulus shows a 2D red ball being launched at the left middle of the screen on a white background. There is no gravity or friction enabled, and no visible boundaries on the white surface. The white surface is flat and featureless, allowing the red ball to travel without obstructions, as shown in Figure 1. We varied the speed at which the ball rolled over the white surface with three different speeds: 100, 300, and 500 (in units of pixels/second). This gives us This gives us 3 stimuli in total. The stimuli and the generated image from the image generation model are in the same resolution (1024*1024) natively.

A.2 2D GRAVITY

The stimulus shows a 2D red ball being launched at various positions (left-middle, left-bottom, right-middle, right-bottom) on a white background. There is gravity enabled, and no visible boundaries on the white surface. The white surface is flat and featureless, allowing the red ball to travel without obstructions, as shown in Figure 1. We varied the speed at which the ball rolled over the white surface with three different speeds: 230, 240, and 250 (in units of pixels/second) and with three different angles: 45° and 60° . This gives us 24 stimuli in total. The stimuli and the generated image from the image generation model are in the same resolution (1024*1024) natively.

A.3 FLUIDS

The stimulus shows a 3D glass mug being filled with water on a light sky-blue background. The water is emitted from a dark-grey pipe into the glass mug, as shown in Figure 1. There is gravity enabled, and the amount of water are limited within a range that it will never overflow. We varied the flow rate: 25, 50, and 75 (in frames/second), the type of cups: small, medium, and large, and the ground truth water levels: 1/12 full, 3/12 full, 5/12 full, 7/12 full, 9/12 full. The stimuli are cropped to 1024*1024 resolution, keeping only the water pipe and the glass water mug. This will give us 45 stimuli in total. The generated images from the image generation model are in the same resolution (1024*1024) natively.

A.4 BOUNCING

The stimulus shows a 3D object being launched from the top and bouncing back after hitting the ground as shown in Figure 1. There is gravity enabled, and the objects all have specific coefficient of restitution. We varied the coefficient of restitution of the object by including various balls made with different materials, and the falling rate. We numbered each object from 1 to 9. Ball 1 is a transparent toy bouncing ball; Ball 2 is a white bouncy ball; Ball 3 is a black bouncy ball; Ball 4 is a squash ball; Ball 5 is a tennis ball; The velocity we varied for these 5 balls includes 25 and 50 (frames / second). Ball 6 is a soccer ball; Ball 7 is a tennis ball; Ball 8 is a purple bouncy ball; Ball 9 is a tennis ball. The velocity we varied for these 5 balls includes 10 and 15 (frames / second). We will also seperate each stimuli into three partitions. The first partition is *before*, which is the sequence of frames that shows the motion of the ball right before it hits the ground and starts to deform; The second partition is *during*, which is the sequence of frames that shows the motion of the ball hitting the ground, deforming, and starts to bounce back; The third partition is *after*, which is the sequence of frames that shows the ball bouncing back upwards. This give us 54 stimuli in total.

The resolution of the stimuli were resized to 1080*720, and the generated images from the image generation model are in 1536*1024, and were resized into 1080*720.

B PROMPTS

For prompt, we designed three parameters for the prompts we used in four domains.

For parameter **number of seconds forward**, which is k, we chose from $k \in [0.2, 0.4, 0.8]$.

For parameter **direction**, we choose from leftbottom, leftmiddle, rightmiddle, and rightbottom.

For parameter **scene content**, we choose it based on the domain. In Fluids, we define the parameter as the following: "a glass mug being filled with water, at a constant rate". For Bouncing, when simulating before and during partitions, we define the parameters as the following: "a bouncy ball falling towards the ground". When simulating after partition, we define the parameters as the following: "a bouncy ball bouncing upward after hitting the ground".

B.1 PROMPT FOR 2D MOTION

In the 2D Motion, for our Chain-of-Time simulation method, as well as our Direct Prediction baseline, models are provided the following prompt, with different methods (Chain-of-Time 0.2s, 0.4s, and Direct Prediction) varying the {{number of seconds forward}} parameter:

Simulation Instruction Prompt

Consider the following 5 frames, which show the motion of a red ball on a white background. Note that each frame is precisely .2 seconds apart.

Now, please generate an image that simulates what this scene would look like {{number of seconds forward}} Seconds into the future.

Make sure that your image is 2d and consists of a single red circle on a solid white background. Ensure that the circle is exactly the same size as the input images. Assume that there is no friction, the ground is flat, and the ball can pass through objects.

{{image sequence}}

For Chain-of-Time, we used the following prompt to elicit subsequent simulation steps from the IGM:

Simulation Follow-Up Prompt

Now, simulate additional {{number of seconds forward}} seconds into the future.

B.2 PROMPTS FOR 2D GRAVITY

In the 2D Gravitydomain, for our Chain-of-Time simulation method, as well as our Direct Prediction baseline, models are provided the following prompt, with different methods (Chain-of-Time 0.2s, 0.4s, and Direct Prediction) varying the {{direction}} and {{number of seconds forward}} parameter:

Simulation Instruction Prompt

Consider the following 5 frames, which show the projectile motion of a red ball being launched from the {direction}. Each frame is precisely 0.2 seconds apart.

You will generate an image that simulates the position of the red ball {number of seconds forward} seconds forward into the future after the last frame.

Assume that there is gravity and the red ball continues to follow the projectile motion shown in the frames provided. The scene is viewed from the side, so gravity pulls downward.

Make sure that the generated image is 2-D, that it contains a circle exactly the same size and color as the circle in the frames provided, and that the background color is white.\

{{image sequence}}

For Chain-of-Time, we use the following prompt to elicit subsequent simulation steps from the IGM:

Simulation Follow-Up Prompt

Generate an additional image that simulates the position of the red ball {number of seconds forward} seconds forward into the future after the last frame that you generated.

Assume that there is gravity and the red ball continues to follow the projectile motion shown in the frames provided. The scene is viewed from the side, so gravity pulls downward.

Make sure that the generated image is 2-D, that it contains a circle exactly the same size and color as the circle in the frames provided, and that the background color is white.\

B.3 PROMPTS FOR FLUIDS AND BOUNCING

In domains Fluids and Bouncing, for our Chain-of-Time simulation method, as well as our Direct Prediction baseline, models are provided the following prompt, with different methods (Chain-of-Time 0.2s, 0.4s, and Direct Prediction) varying the {{scene content}} and {{number of seconds forward}} parameter:

Simulation Instruction Prompt

Consider the following sequence of 5 images, which show { scene_content}. Each image frame video is precisely 0.2 seconds after the last frame.

Please generate an image that continues this sequence, simulating what the scene will look like {number of seconds forward} seconds further into the future after the last frame. Make sure that the generated image is from exactly the same perspective as the input images and that the background color remains the same color.

{{image sequence}}

For Chain-of-Time, we use the following prompt to elicit subsequent simulation steps from the IGM:

Simulation Follow-Up Prompt

Continue simulating this scene {number of seconds forward} seconds into the future after the last frame that you generated. Make sure that the generated image is from exactly the same perspective as the input images and that the background color remains the same color.

C COMPUTER VISION ALGORITHMS USED FOR OBJECT DETECTION IN ALL FOUR DOMAINS

C.1 THE 2D MOTIONAND 2D GRAVITY DOMAINS

The CV algorithms we used to detect the red ball in the images generated by the image models are coded by ChatGPT-5. The code description provided by the model is as follow:

Purpose. Detect the centroid of the largest red region in an image.

Steps.

- 1. Read the image at frame_path (BGR) and convert it to HSV, since hue-based thresholding is more robust than RGB for color detection.
- 2. Define two HSV ranges for red (red wraps around the hue wheel), covering low hue (0–10) and high hue (170–180) with saturation/value floors to avoid dark or washed-out pixels:

$$\begin{aligned} & \text{lower_red}_1 = (0, 70, 50), & \text{upper_red}_1 = (10, 255, 255), \\ & \text{lower_red}_2 = (170, 70, 50), & \text{upper_red}_2 = (180, 255, 255). \end{aligned}$$

- 3. Threshold the HSV image with both intervals and OR the results to obtain a binary mask of red pixels.
- 4. Find external contours on the mask. If none are found, return (None, None).
- 5. Select the largest contour by area (assumes the main red target is the biggest red blob in view).
- 6. Compute spatial moments for that contour. If $m_{00}=0$ (degenerate area), return (None, None); otherwise compute the centroid:

$$c_x = \frac{m_{10}}{m_{00}}, \qquad c_y = \frac{m_{01}}{m_{00}}.$$

7. Return (c_x, c_y) as integer pixel coordinates. If no valid region exists, return (None, None).

Returns. (int, int) or (None, None): the centroid of the largest red region, or None/None when no suitable red region is found.

And figure 8 are examples of the algorithm detecting the red ball in images generated in 2D Motion, and 2D Gravity.

C.2 THE FLUIDS DOMAIN

The CV algorithms we used to detect the water blob and water level in the images generated by the image generation models are coded by ChatGPT-5. The code description provided by the model is as follow:

Detect the water "blob" inside a glass mug and report its top/bottom y.

Inputs

- IGM_path: path to RGB/RGBA image.
- y_cut: only analyze rows $y \ge y_cut$ (ignore the upper part of the image).
- alpha_thresh: pixels with alpha ≤ this are treated as transparent (ignored).
- hsv_lower/hsv_upper: HSV thresholds for sky-blue liquid (OpenCV $H \in [0, 179]$).
- erode_iters, close_kernel: morphology parameters to suppress thin rims/stream and fill gaps.
- coverage_main / coverage_fallback: minimum horizontal coverage (fraction of bbox width) required for a row to be considered liquid; a fallback is used if the main threshold yields none.

ullet ignore_top_rows: discard the first N rows inside the ROI to avoid picking the crop boundary.

Steps

- 1. Read the image with cv2.IMREAD_UNCHANGED so the alpha channel (if present) is preserved.
- 2. Build an alpha mask: alpha_mask = $(\alpha > \text{alpha_thresh})$. If no alpha channel exists, use an all-ones mask (all pixels opaque).
- 3. Crop to the region of interest (ROI): rows $y \ge y _cut$. Crop the alpha mask the same way.
- 4. Convert the ROI to HSV and threshold with [hsv_lower, hsv_upper] to obtain a binary color mask for the sky-blue liquid.
- 5. AND the color mask with the alpha mask to suppress fully/mostly transparent background.
- 6. Morphological cleanup:
 - Erode (erode_iters times) to remove thin bright rims and the pouring stream.

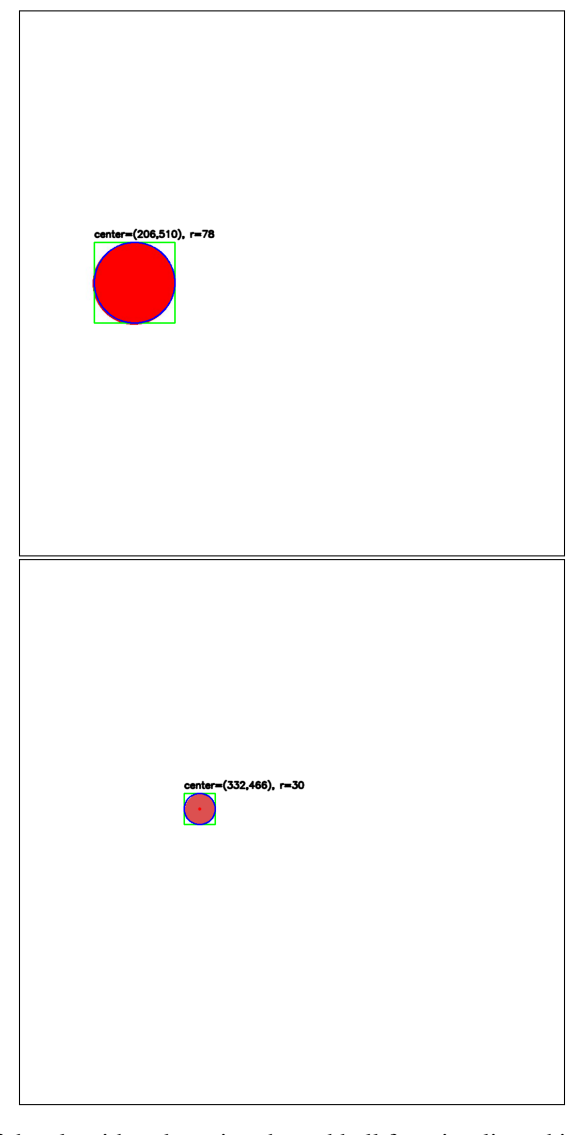


Figure 8: Examples of the algorithm detecting the red ball for stimuli used in 2D Motion, and 2D Gravity.

- Close (kernel size = close_kernel) to reconnect the eroded blob and fill small holes.
- 7. Find connected components (external contours) and select the largest-area component as the liquid blob.
- 8. Compute the blob's bounding box (x, y, w, h) in ROI coordinates. Inside this box:
 - For each row, count foreground pixels (row_counts).
 - Mark rows as liquid if row_counts \geq coverage_main $\times w$.
 - If none qualify, relax to coverage_fallback $\times w$.
 - Discard candidate rows whose index < ignore_top_rows.
- 9. Determine water-level bounds:
 - Top y (global) = y_cut + y + min(valid_row_indices) if valid rows exist; otherwise y_cut + min(contour_y).
 - Bottom y (global) = y_cut + y + max(valid_row_indices) if valid rows exist; otherwise y_cut + max(contour_y).
- 10. Optional visualization:
 - Red rectangle: blob bounding box.
 - Green line: top *y*. Blue line: bottom *y*.

Notes

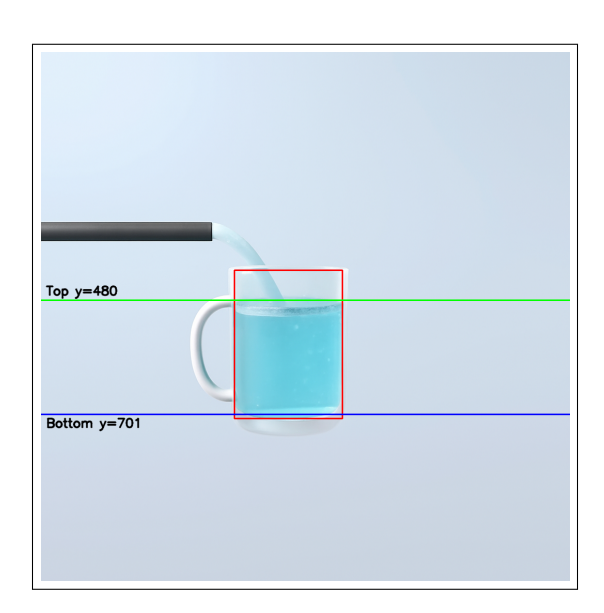


Figure 9: Examples of the algorithm detecting the water level for stimuli used in Fluids.

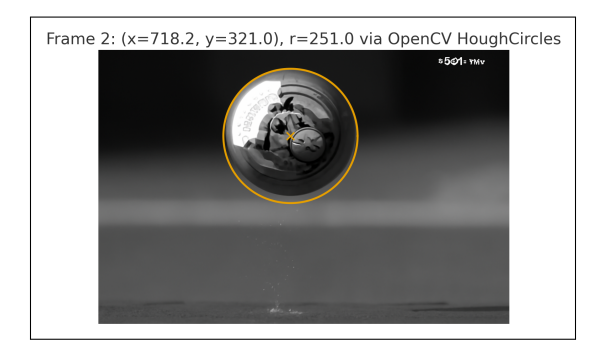


Figure 10: Examples of the algorithm detecting the ball used in Bouncing.

- HSV bounds are intentionally broad; tune to lighting and hue variations.
- Erosion suppresses 1–2 px rims and stream artifacts that otherwise bias the "top" level.
- The row-coverage rule prefers rows where a substantial horizontal span is filled, making the estimate robust to foam/splash highlights.
- Complexity is approximately O(HW) per frame (thresholding + morphology + a single bbox scan).

And figure 9 is an example of the algorithm detecting the water level in images generated in Fluids.

C.3 THE BOUNCING DOMAIN

The CV algorithms we used to detect the ball in the images generated by the image models are coded by ChatGPT-5. The code description provided by the model is as follow:

We detect a single ball in an RGB image using a two-stage strategy: (i) a Hough transform for circles on a contrast-enhanced, downscaled grayscale image; and (ii) a fallback based on contour circularity if no reliable Hough detection is found. The routine computes both a bounding box and a center, clamps the box to image bounds, and returns the center.

Inputs. An image $\mathbf{I} \in \mathbb{R}^{H \times W \times 3}$ (BGR order as in OpenCV).

Outputs. Center (c_x, c_y) in original-image pixel coordinates. (Note: the code also computes a bounding box (x, y, w, h) but, as written, returns only the center.)

Preprocessing.

- 1. Downscale I by $2\times$ (area interpolation) to reduce noise and speed up detection.
- 2. Convert to grayscale and apply CLAHE (clip limit = 2.0, tile size 8×8) for local contrast amplification, followed by Gaussian blur (kernel 7×7 , $\sigma \approx 1.5$) to suppress noise.

Stage 1: Hough circle detection.

• Apply HoughCircles (gradient method) with parameters:

$$dp = 1.2$$
, $minDist = 50$, $param1 = 100$, $param2 = 18$, $r \in [15, 200]$.

- If one or more circles are found, choose the one with the strongest edge response. For each candidate $(\tilde{c}_x, \tilde{c}_y, \tilde{r})$, compute a thin ring mask and measure the mean Canny edge magnitude within the ring; select the circle with the maximal mean.
- Rescale $(\tilde{c}_x, \tilde{c}_y, \tilde{r})$ by factor 2 back to original resolution: $(c_x, c_y, r) = (2\tilde{c}_x, 2\tilde{c}_y, 2\tilde{r})$.
- Define a square bounding box centered at (c_x, c_y) with side length 2r: $(x, y, w, h) = (c_x r, c_y r, 2r, 2r)$.

Stage 2 (fallback): contour circularity.

- 1. If Hough detection fails, convert the original image to grayscale, blur (Gaussian 7×7), and compute Canny edges.
- 2. Morphological close with a 5×5 kernel to connect fragmented edges.
- 3. Extract external contours and filter:
 - Reject small contours: area A < 300 px.
 - Compute perimeter P and circularity

$$C = \frac{4\pi A}{P^2 + \epsilon}, \quad \epsilon = 10^{-6};$$

keep contours with $C \geq 0.7$.

- 4. For each remaining contour, compute the axis-aligned bounding box (x, y, w, h) and score it by $C \cdot A$; take the maximum-scoring contour as the ball.
- 5. Set center $(c_x, c_y) = (x + \lfloor w/2 \rfloor, y + \lfloor h/2 \rfloor)$ and approximate radius $r = \lfloor \max(w, h)/2 \rfloor$.

Post-processing. Clamp (x,y,w,h) to image bounds: $x \leftarrow \max(0,x), \ y \leftarrow \max(0,y), \ w \leftarrow \min(w,W-x), \ h \leftarrow \min(h,H-y)$. Return the integer center (c_x,c_y) .

Notes and implementation details.

- Contrast-limited histogram equalization (CLAHE) improves robustness to faint or lowcontrast balls.
- The edge-strength tie-breaker favors circles with sharper boundaries rather than merely high accumulator votes.
- The circularity threshold $\mathcal{C} \geq 0.7$ trades off recall vs. precision; higher values reject more elongated shapes.
- If no suitable contour is found, the routine raises an exception (''Ball not found'').
- *Docstring mismatch:* the docstring claims to return both bounding box and center, but the function currently returns only the center; adjust as needed.

And figure 10 is an example of the algorithm detecting the ball in images generated in Bouncing.

D ADDITIONAL ANALYSIS

D.1 THE 2D GRAVITY DOMAIN

Here are the additional analysis for stimuli with speed 230 pixels/second, angle 60° , and launching position left-bottom. We present the result generated by Chain-of-time 0.4s on the same stimuli. We can see that we observed the deceleration on the y-axis due to gravity, and we can see the projectile motion like curve on the left plot of the figure 11, matching the conclusion we reached in section 5.2.2.

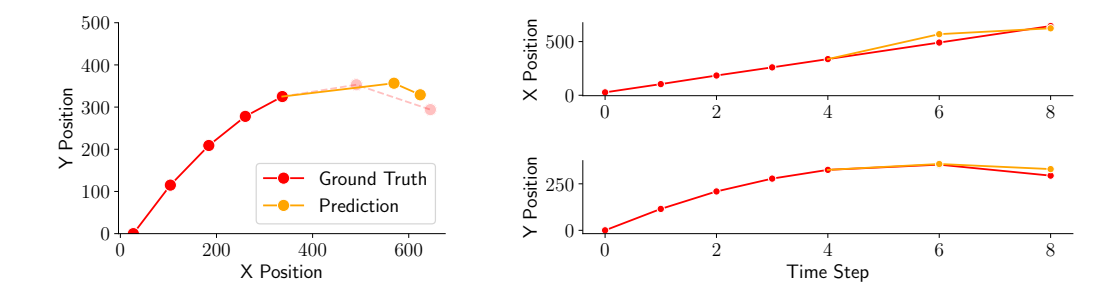


Figure 11: Predicted projectile position for 2D Gravityover time for a single trial using Chain-of-Time 0.4s. Red represents the ground truth ball location and orange is the simulated ball location at each time step, averaged across 20 samples. (Left) Projectile location in (x,y) coordinate space (Right) Predicted x-location and y-location as a function of time.

Here are the additional analysis for stimuli with speed 240 pixels/second, angle 60° , and launching position left-bottom. We present the result generated by Chain-of-Time 0.2s on the same stimuli. We can see that we observed the deceleration on the y-axis due to gravity, and we can see the projectile motion like curve on the left plot of the figure 12, matching the conclusion we reached in section 5.2.2.

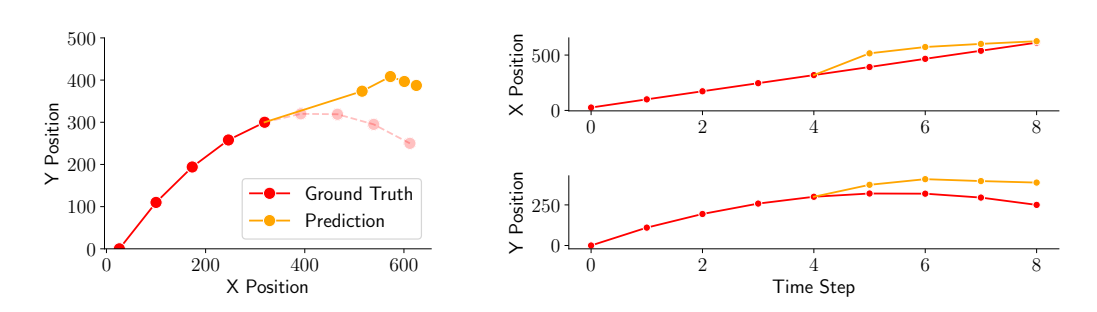


Figure 12: Predicted projectile position for 2D Gravityover time for a single trial using Chain-of-Time 0.2s. Red represents the ground truth ball location and orange is the simulated ball location at each time step, averaged across 20 samples. (Left) Projectile location in (x,y) coordinate space (Right) Predicted x-location and y-location as a function of time.

Here are the additional analysis for stimuli with speed 240 pixels/second, angle 60° , and launching position left-bottom. We present the result generated by Chain-of-Time 0.4s on the same stimuli. We can see that we observed the deceleration on the y-axis due to gravity, and we can see the projectile motion like curve on the left plot of the figure 13, matching the conclusion we reached in section 5.2.2.

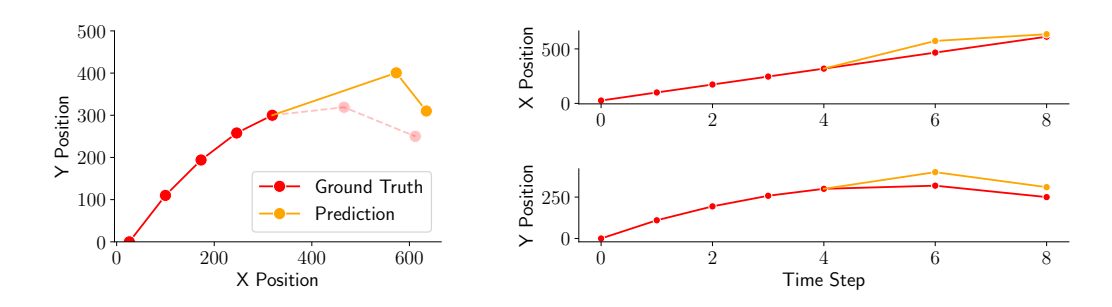


Figure 13: Predicted projectile position for 2D Gravityover time for a single trial using Chain-of-Time 0.2s. Red represents the ground truth ball location and orange is the simulated ball location at each time step, averaged across 20 samples. (Left) Projectile location in (x,y) coordinate space (Right) Predicted x-location and y-location as a function of time.

Here are the additional analysis for stimuli with speed 220 pixels/second, angle 60° , and launching position right-middle. We present the result generated by Chain-of-Time 0.2s on the same stimuli. We can see that we observed the deceleration on the y-axis due to gravity, and we can see the projectile motion like curve on the left plot of the figure 14, matching the conclusion we reached in section 5.2.2.

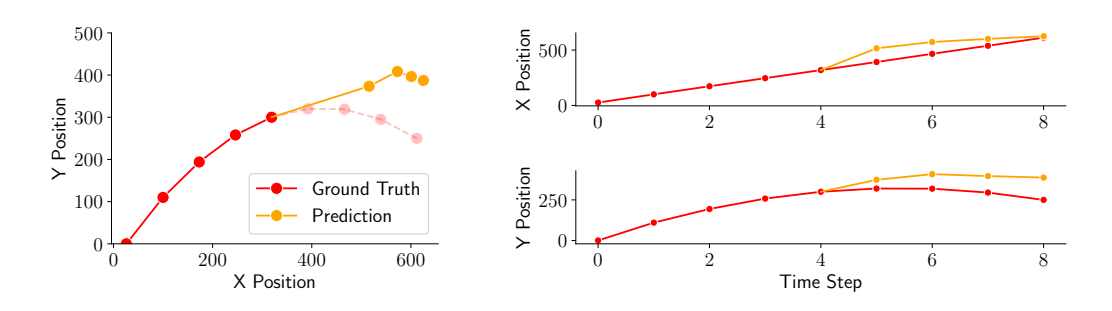


Figure 14: Predicted projectile position for 2D Gravityover time for a single trial using Chain-of-Time 0.2s. Red represents the ground truth ball location and orange is the simulated ball location at each time step, averaged across 20 samples. (Left) Projectile location in (x,y) coordinate space (Right) Predicted x-location and y-location as a function of time.

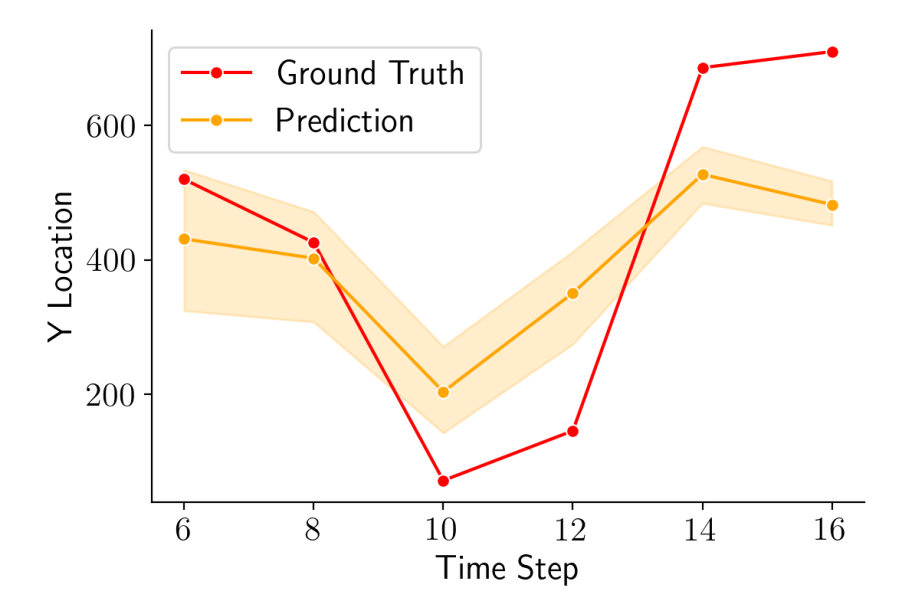


Figure 15: Simulated ball location (orange) using Chain-of-Time 0.4s in the Bouncing domain follow a similar U-shaped curve as the ground truth ball location (red). Ball locations are shown here for a single video (orange), with predictions aggregated across all samples for the three time periods (before/during/after collision).

D.2 THE BOUNCING DOMAIN

Here are the additional analysis on data generated by Chain-of-Time 0.2s and 0.4s for ball 2 at velocity 50 frames/second. This is the result generated by Chain-of-Time 0.4s simulation. We can see that the bouncing motion is shown by the deep V shaped curved, and the IGM underestimated the coefficient of restitution, since IGM thinks the ball is bouncing back slower, which the conclusion matches with the conclusion we reached in section 5.2.2

Here are the additional analysis on data generated by Chain-of-Time 0.2s and 0.4s for ball 4 at velocity 50 frames/second. We can see that the bouncing motion is shown by the deep V shaped curved, and the IGM underestimated the coefficient of restitution in Chain-of-Time 0.4s, since IGM thinks the ball is bouncing back slower.

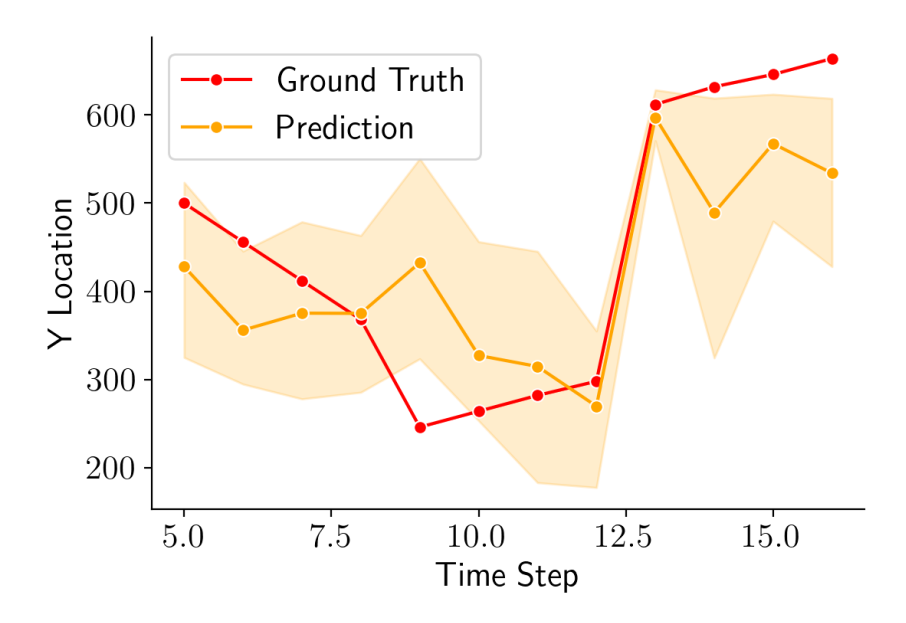


Figure 16: Simulated ball location (orange) using Chain-of-Time 0.2s in the Bouncing domain follow a similar U-shaped curve as the ground truth ball location (red). Ball locations are shown here for a single video (orange), with predictions aggregated across all samples for the three time periods (before/during/after collision).

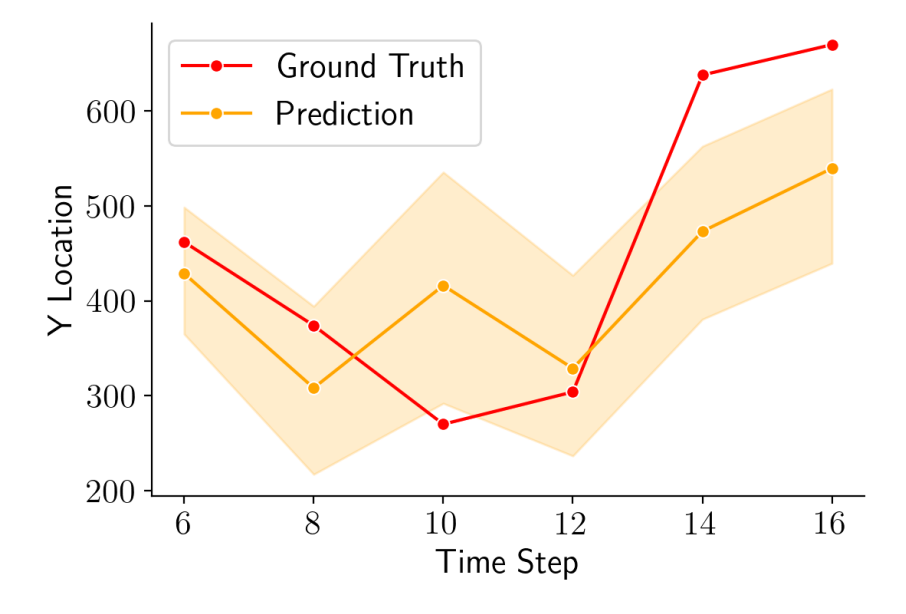


Figure 17: Simulated ball location (orange) using Chain-of-Time 0.4s in the Bouncing domain follow a similar U-shaped curve as the ground truth ball location (red). Ball locations are shown here for a single video (orange), with predictions aggregated across all samples for the three time periods (before/during/after collision).

Here are the additional analysis on data generated by Chain-of-Time 0.2s and 0.4s for ball 7 at velocity 15 frames/second. We can see that the bouncing motion is shown by the deep V shaped curved, and the IGM underestimated the coefficient of restitution, since IGM thinks the ball is bouncing back slower.

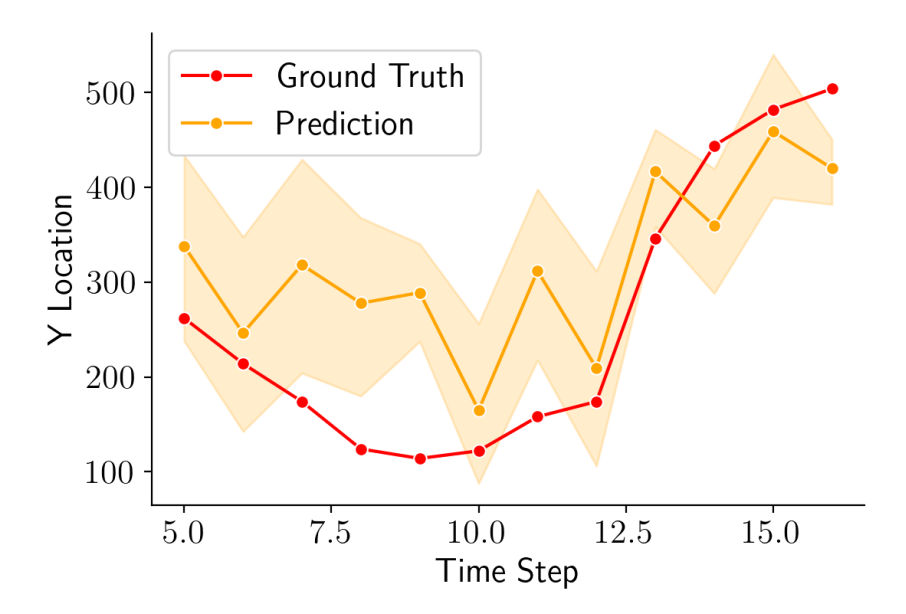


Figure 18: Simulated ball location (orange) using Chain-of-Time 0.2s in the Bouncing domain follow a similar U-shaped curve as the ground truth ball location (red). Ball locations are shown here for a single video (orange), with predictions aggregated across all samples for the three time periods (before/during/after collision).

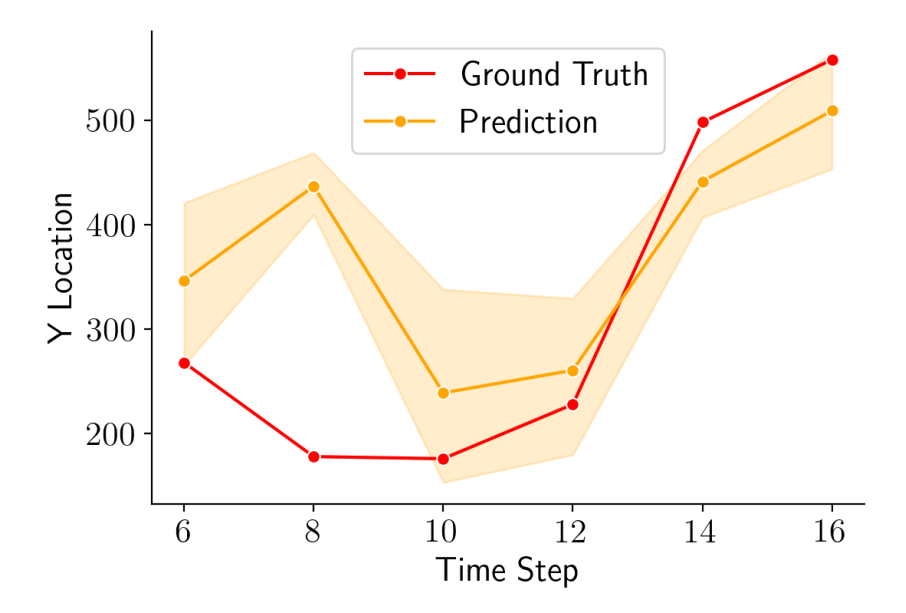


Figure 19: Simulated ball location (orange) using Chain-of-Time 0.4s in the Bouncing domain follow a similar U-shaped curve as the ground truth ball location (red). Ball locations are shown here for a single video (orange), with predictions aggregated across all samples for the three time periods (before/during/after collision).

Here are the additional analysis on data generated by Chain-of-Time 0.2s and 0.4s for ball 9 at velocity 10 frames/second. We can see that the bouncing motion is shown by the deep V shaped curved, and the IGM underestimated the coefficient of restitution, since IGM thinks the ball is bouncing back slower.

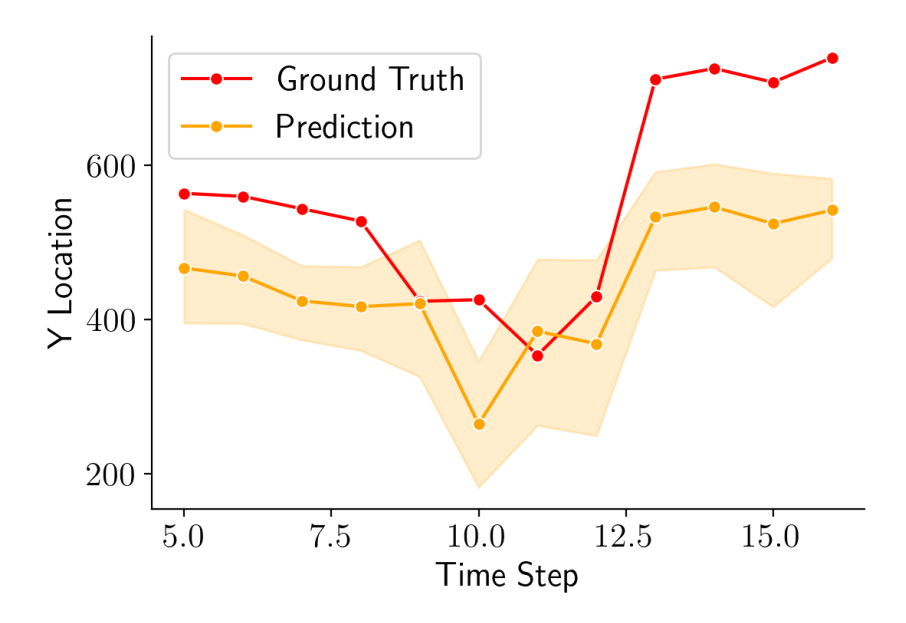


Figure 20: Simulated ball location (orange) using Chain-of-Time 0.2s in the Bouncing domain follow a similar U-shaped curve as the ground truth ball location (red). Ball locations are shown here for a single video (orange), with predictions aggregated across all samples for the three time periods (before/during/after collision).

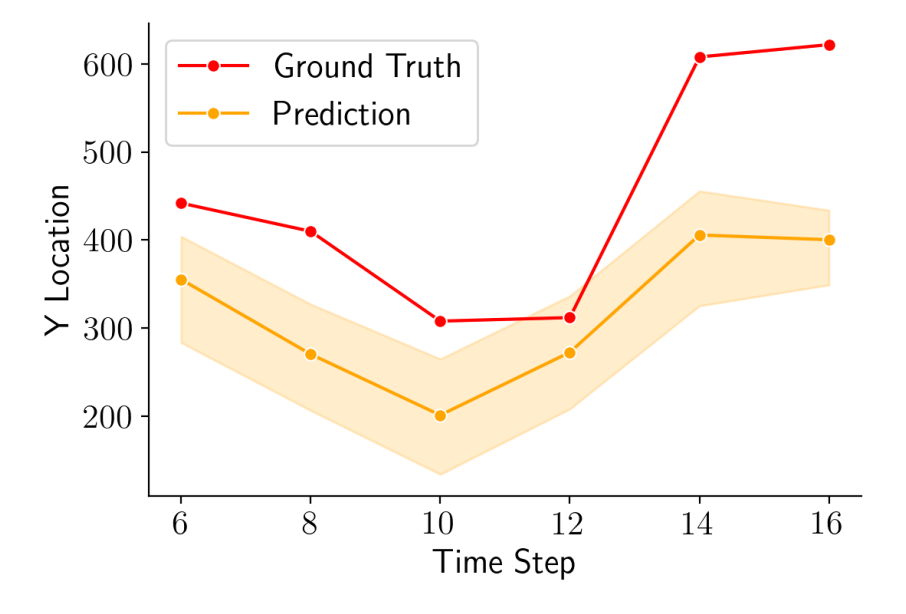


Figure 21: Simulated ball location (orange) using Chain-of-Time 0.4s in the Bouncing domain follow a similar U-shaped curve as the ground truth ball location (red). Ball locations are shown here for a single video (orange), with predictions aggregated across all samples for the three time periods (before/during/after collision).

E LANGUAGE MODEL STATEMENT

LLMs were used in this work for literature review and for coding assistance with constructing computer vision algorithms described in Appendix C.3